Large-scale electrochemical synthesis of SnO$_2$ nanoparticles

Wei Chen · Debraj Ghosh · Shaowei Chen

Abstract Tin oxide nanoparticles were synthesized by electrochemical oxidation of a tin metal sheet in a non-aqueous electrolyte containing NH$_4$F. The as-prepared nanoparticles were then thermally annealed at 700 °C for 6 h. The resulting particles were characterized by a variety of experimental techniques, including X-ray diffraction (XRD), high-resolution transmission electron microscopy (HRTEM), Raman, UV-visible, and photoluminescence (PL) spectroscopy. The XRD patterns clearly showed that the amorphous phase of the as-synthesized SnO$_2$ particles was transformed into a rutile-type crystalline structure after thermal treatment; and from the line broadening of the XRD peaks, the average size of the annealed particles was found to be 15.4, 12.5, 11.8 nm for the particles initially synthesized at 20, 30, and 40 V, respectively. Consistent results were also observed in HRTEM measurements which showed clear crystalline lattice fringes of the calcined nanoparticles, as compared to the featureless profiles of the as-produced counterparts. In Raman spectroscopic studies, three dominant peaks were observed at 480, 640, and 780 cm^{-1} which were ascribed to the E$_{1g}$, A$_{1g}$, and B$_{2g}$ Raman active vibration modes, respectively, and the wavenumbers of these peaks blue-shifted with decreasing particle size. Additionally, a broad strong emission band was observed in room-temperature photoluminescence measurements.

W. Chen · D. Ghosh · S. Chen (✉)
Department of Chemistry and Biochemistry, University of California, 1156 High Street, Santa Cruz, CA 95064, USA
e-mail: schen@chemistry.ucsc.edu

Introduction

Transition-metal oxide nanomaterials, such as ZnO, TiO$_2$, WO$_3$, and SnO$_2$, have attracted extensive research interests owing to their unique physical and chemical properties and diverse potential applications in optical and electronic fields. Of these, tin oxide (SnO$_2$) with the rutile structure is a promising functional *n*-type semiconductor material with a wide band-gap (E_g = 3.65 eV at 300 K), which has been used extensively in energy storage and conversion (for instance, solar cells and lithium ion batteries) [1–3], catalysis [4–6], gas sensors [7–11], transparent conducting electrodes [12], and optoelectronic devices [13–15].

To date, a wide variety of SnO$_2$ nanomaterials with interesting structures and properties have been prepared, such as nanoparticles [16–19], nanorods [20–22], nanotubes [3], nanowires [9, 23], nanobelts [8, 24, 25], and hollow spheres [26, 27]. The typical synthetic approaches entail sol–gel processes [2, 11, 28, 29], vapor-liquid-solid (VLS) growth [25, 30, 31], chemical vapor deposition [32–34], sputtering [35, 36], and solution phase growth [7, 37–39]. In these, high temperature and/or vacuum are generally required, along with complicated pre- and post-synthesis processing. For instance, in most of these strategies, surfactants or organic polymers are used to control the dimensions and morphologies of the SnO$_2$ nanomaterials. Yet, prior to practical applications, these organic impurities typically have to be removed, and such processing may lead to complication of the particle size, surface area, and stability of the particles. In the traditional solution phase growth methods [7, 37–39], the by-products may also compromise the material purity. Thus, it is important to develop an effective strategy to prepare pure tin oxide nanomaterials with high efficiency and under mild conditions from the viewpoints of both fundamental

research and practical applications. To this end, electrochemical techniques have proven to be very effective, which in recent years have been employed to prepare size and shape controlled (alloy) metal (e.g., Pd, NiPd, FeCo, etc.) [40, 41] and metal oxide [42–44] nanoparticles. In these methods, simple two-electrode setups are used and the metal anodes are offered as a sacrificial source for metal or metal oxide nanoparticles. The advantages of these electrochemical routes lie in the simplicity, convenience, and the generation of pure, homogeneous, and large quantities of particles.

In this article, we report a simple one-step route based on electrochemical oxidation of a tin metal sheet to the preparation of a large quantity of SnO_2 nanoparticles in a non-aqueous electrolyte containing NH_4F. In recent years, various fluoride compounds such as HF, NH_4F, NaF, and KF have been used as effective etching reagents in the synthesis of highly ordered arrays of TiO_2 nanotubes by the anodic oxidation method [45–47]. This is to take advantage of the enhanced electrochemical dissolution of TiO_2 in the presence of fluoride ions. In the present study, the etching characteristics of fluoride electrolytes were exploited for the preparation of SnO_2 nanoparticles by electrochemical dissolution of a tin metal sheet. The particle size was found to be controlled by the applied voltage. Effects of thermal treatments on the particle crystalline structure were then examined by a wide array of spectroscopic techniques.

Experimental section

Tin foil (0.25 mm thick, 99.8% purity (metal basis)) and ethylene glycol (99+%) were purchased from Aldrich. Ammonium fluoride (NH_4F, 98+%, extra pure) was purchased from ACROS. These were all used without further treatment. Before the experiments, the tin sheet was degreased by sonication in acetone, ethanol, and Nanopure water successively and then dried in nitrogen. The SnO_2 nanoparticles were prepared by using a simple two-electrode (2 cm separation) cell in which the tin foil was used as the sacrificial anode and a Pt coil as the cathode, along with a non-aqueous electrolyte consisting of 74 mM NH_4F in ethylene glycol. In a typical experiment, around 10 g of SnO_2 nanoparticles were produced in each batch. All the electrochemical reactions were carried out at room temperature using a DC regulated power supply (B&K Precision Corp., 1623A, output voltage 0–60 V) in the constant voltage mode. Three samples were prepared by varying the applied voltage at 20, 30, and 40 V, respectively. After the reactions, the resulting white powders were centrifuged and thoroughly washed with Nanopure water and absolute ethanol for several times and dried at room temperature. The dried powders were then calcined in

air at 700 °C for 6 h with the heating and cooling rates controlled at 5 °C/min to convert the amorphous phase to the crystalline one.

Powder X-ray diffraction (XRD) was performed on a Rigaku Mini-flex Powder Diffractometer using Cu-Kα radiation with a Ni filter ($\lambda = 0.154059$ nm at 30 kV and 15 mA). The average particle size was calculated from the X-ray line broadening of the (110) and (101) diffraction peaks by using the Debye–Scherrer equation (in the calculations, the instrumental broadening was taken into account, which was calibrated with standard Si samples). High-resolution transmission electron microscopic (HRTEM) images were collected with a Phillips CM200/FEG (field-emission gun) electron microscope operated at an accelerating voltage of 200 kV. TEM samples were prepared by depositing a drop of a dilute SnO_2 dispersion in ethanol onto a carbon-coated copper grid. Raman scattering spectra were acquired using an RM series Renishaw microscope with a 50 mW diode laser at 780 nm. Renishaw's WiRE (Windows-based Raman Environment) proprietary software with Galactic Industries GRAMS/32 C software was used for data collection and analysis. The SnO_2 samples were visualized under white light and then Raman scattering data were collected between 100 and 3000 cm^{-1}. Prior to each measurement, a Si wafer was used to calibrate the Raman equipment by the characteristic band at 520 cm^{-1}. Photoluminescence (PL) studies were carried out with a PTI fluorescence spectrometer and UV-Vis spectra were collected by using an ATI UNICAM UV4 spectrometer.

Results and discussion

To examine the effects of thermal annealing on the particle crystalline structures, powder X-ray diffraction measurements were first carried out. Figure 1 shows the XRD patterns of the SnO_2 nanoparticles prepared at different voltages (20, 30, and 40 V) before and after thermal treatments. The JCPDS data of SnO_2 (cassiterite) is also included in the figure (curve a). It can be seen that the as-prepared SnO_2 samples (curve b, represented by the one synthesized at 40 V; others show similar results) exhibit only featureless profiles with two (weak) broad peaks at ca. $2\theta = 30°$ and 58°, signifying an amorphous phase of the materials. However, after thermal annealing at 700 °C for 6 h, all three samples (curves c–e) show clear, sharp, and strong diffraction peaks that are in excellent agreement with the tetragonal structure (rutile type) of SnO_2 in JCPDS No. 41-1445 (curve a), with the lattice constants of $a = 4.738$ Å and $c = 3.187$ Å. This strongly suggests the transformation of the particles into a crystalline form. Additionally, no diffraction features that are characteristic

Fig. 1 XRD patterns of (a) bulk SnO$_2$ from the Joint Committee Powder Diffraction Standard (JCPDS) No. 41-1445; (b) the as-prepared SnO$_2$ particles at 40 V; and the annealed particles that were initially synthesized at different voltages: (c) 20 V, (d) 30 V, and (e) 40 V
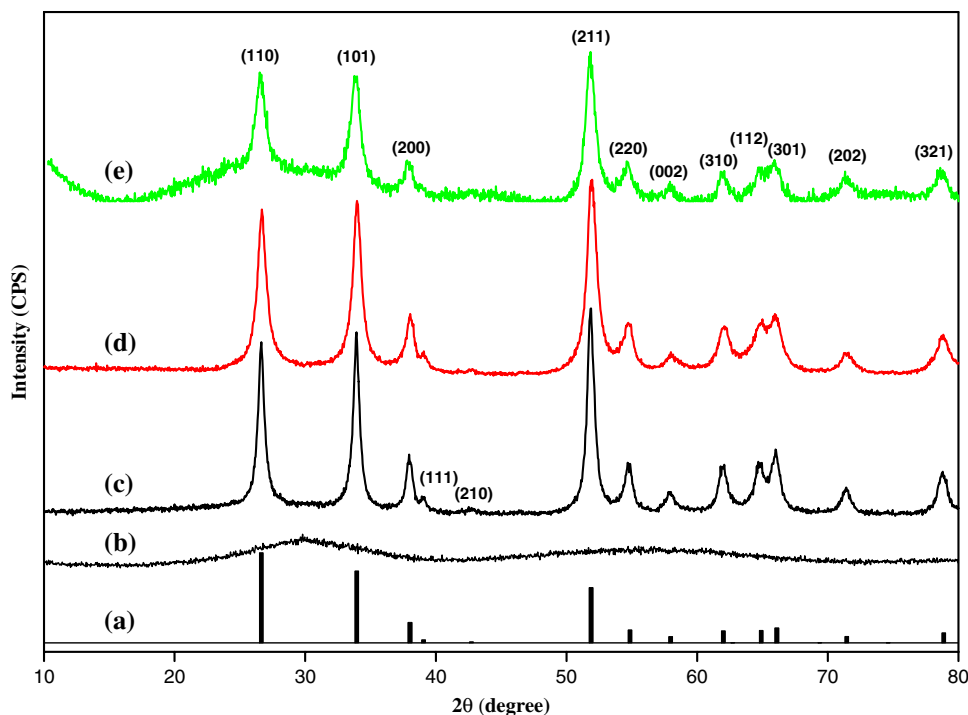
of impurities such as unreacted Sn and other tin oxides phases were observed, indicating the purity of the SnO$_2$ nanocrystals.

From the XRD patterns in curves c–e, it can be seen that the diffraction peaks are broadened in comparison with those from bulk materials (curve a). This is attributable to the small size of the SnO$_2$ particles. In fact, the average size of the SnO$_2$ particles can be estimated by the Debye–Scherrer equation, $D = K\lambda/\beta \cos \theta$, where D is the diameter of the nanoparticles, $K = 0.9$, λ (Cu-Kα) = 1.54059 Å, and β is the full width at half maximum of the diffraction peaks. Based on the (110) and (101) diffraction peaks, the average size was found to be 15.4, 12.5, 11.8 nm for the SnO$_2$ nanoparticles that were initially synthesized at 20, 30, and 40 V, respectively. Clearly, the particle size decreases with increasing electrode voltage during the electrochemical synthesis. This can be understood on the basis of the particle growth mechanism that may be represented by the following three steps, with the oxygen supplied by the electro-splitting of water (step 2),

$$Sn \rightarrow Sn^{4+} + 4e^- \tag{1}$$

$$2H_2O \rightarrow 4H^+ + O_2 + 4e^- \tag{2}$$

$$Sn^{4+} + O_2 + 4e^- \rightarrow SnO_2 \tag{3}$$

By increasing the applied electrode voltage, the anodic generation of Sn^{4+} will be accelerated (step 1), leading to an increase of the nucleation sites for oxide particle formation and hence decreasing particle dimensions (step 3). In other words, electrode voltages can be exploited as an effective variable in the manipulation of the particle size.

Furthermore, it can be seen from Fig. 1 that, for the samples prepared at 20 and 30 V, the XRD profiles also exhibit two additional weak peaks for the (111) and (210) diffraction planes, whereas they are indiscernible for the sample synthesized at 40 V. This discrepancy can again be ascribed to the line broadening effect because of the small particle size. Table 1 summarizes the peak position, lattice spacing (d), and ratios of the peak intensity of the three strongest XRD peaks (I_{101}/I_{110} and I_{211}/I_{110}) for SnO$_2$

Table 1 XRD peak position (2θ), lattice spacing (d), and ratio of peak intensity of the three SnO$_2$ nanoparticle samples

Samples	(110)		(101)			(211)		
	2θ	d_{hkl} (nm)	2θ	d_{hkl} (nm)	I_{101}/I_{110}	2θ	d_{hkl} (nm)	I_{211}/I_{110}
SnO$_2$ (JCPDS)	26.63	0.3347	33.95	0.2640	0.80	51.88	0.1762	0.61
SnO$_2$ (20 V)	26.64	0.3344	33.91	0.2641	1.08	51.87	0.1761	1.24
SnO$_2$ (30 V)	26.68	0.3339	33.96	0.2638	1.06	51.85	0.1762	1.14
SnO$_2$ (40 V)	26.52	0.3358	33.95	0.2638	1.09	51.84	0.1762	1.54

nanoparticles prepared at different voltages, along with standard data for bulk SnO_2 from JCPDS. One can see that the peak positions and lattice spacing exhibit no appreciable difference between the three particle samples and the bulk standard. In contrast, the ratios of I_{101}/I_{110} and I_{211}/I_{110} for bulk SnO_2 are both less than 1, whereas for the three particle samples, the ratios are all larger than 1. This observation seems to indicate that the [101] and [211] orientations become increasingly dominant in nanosized SnO_2 particles, and more so for the SnO_2 nanoparticles prepared at higher electrode voltages. That is, the present study seems to provide a simple method to synthesize SnO_2 nanoparticles with abundant [101] and [211] orientations. It should be noted that in previous studies of SnO_2 films prepared by the CVD method, the [200] orientation was found to be predominant [48].

To further characterize the particle morphology, TEM studies were then carried out. Figure 2 displays the low-resolution TEM micrographs of the three samples before and after thermal annealing. First, rather uniform particles can be seen in the as-synthesized SnO_2 samples, which appear to agglomerate into an aggregate structure with a cross section of 40–50 nm in diameter and a somewhat rough surface morphology (panels a, c, and e). After sintering at 700 °C (panels b, d, and f), the particle aggregates can be seen to shrink rather substantially into a highly crystalline form, and concurrently the diameter decreases to only 10–15 nm, very consistent with those estimated from XRD measurements (vide ante)—more details can be seen in Fig. 3. Furthermore, the surface roughness is also significantly reduced. Interestingly, nanorods/nanotubes can also be observed with the samples prepared at 20 V (marked with circles in panel b), though the density is very low. In both cases, because of the lack of stabilizing surfactants, extensive agglomeration of particles can be seen.

The evolution of the particle crystallinity was then examined by HRTEM studies, which shows consistent results with the XRD data (Fig. 1). Before thermal annealing, the three particle samples (Fig. 3a, c, and e) exhibit no crystalline feature, in agreement with the amorphous nature of the particles as manifested in XRD measurements (Fig. 1b). Additionally, it can be seen that the aggregates observed in low-resolution TEM images (Fig. 2) indeed consist of a porous network of particles of 2–3 nm in diameter. In sharp contrast, after sintering at 700 °C, all three particle samples exhibit very well-defined crystalline lattice fringes (Fig. 3b, d, and f). For instance, as marked in the HRTEM micrographs (Fig. 3), interplanar spacings of 0.33 and 0.26 nm can be clearly observed, which correspond to the (110) and (101) planes of rutile SnO_2, respectively. Note that in XRD measurements (Fig. 1c–e), the peaks from these two diffractions are also most intense. Also, twin structures may be found, as

highlighted in panel d. Twinning is a characteristic feature of the coalescent grains. The straight twin boundaries are coherent and consist of Sn atoms shared by the two neighboring components of the twin [49]. This experimental feature is in line with the collapse of the originally amorphous particles and the resulting shrinkage of the particle aggregates as observed in Fig. 2.

Further insights into the particle structure were obtained by Raman scattering measurements. Figure 4 shows the room-temperature Raman scattering spectra of the three annealed SnO_2 nanoparticles. In general, SnO_2 with the rutile structure belongs to the space group of D_{4h}, of which the normal lattice vibration at the Γ point of the Brillouin zone is given on the basis of group theory [50, 51]

$$\Gamma = 1A_{1g} + 1A_{2g} + 1A_{2u} + 1B_{1g} + 1B_{2g} + 2B_{1u} + 1E_{1g} + 3E_u \tag{4}$$

Among these vibrations, A_{1g}, B_{1g}, B_{2g}, and E_{1g} are Raman-active modes, and symmetrical A_{2u} and E_u are infrared-active. However, the symmetrical A_{2g} and B_{1u} are optically inactive. The three fundamental Raman peaks at around 480, 640, and 780 cm^{-1} in Fig. 4 (right panel) are therefore ascribed to the E_{1g}, A_{1g}, and B_{2g} vibration modes of the rutile SnO_2, respectively. It can also be seen from the figure that the A_{1g} mode has the strongest Raman intensity, followed by the B_{2g} and E_{1g} modes, in good agreement with those observed in previous studies [15, 20, 32, 52, 53]. The Raman studies further confirm that the calcined SnO_2 nanoparticles prepared above exhibit a tetragonal rutile structure. However, the Raman signal from B_{1g} mode cannot be observed because of the very low intensity (e.g., $I(A_{1g})/1000$) [54]. In addition to the three strong peaks, there is another weak peak at around 694 cm^{-1} for all the three particle samples, which is assigned to the IR-active A_{2u} LO mode (the mode of the longitudinal optical phonons) [53].

The peak positions corresponding to the E_{1g}, A_{1g}, and B_{2g} vibration modes of the three samples are summarized in Table 2, along with those of bulk SnO_2 [53]. It can be clearly seen that the Raman frequencies of the annealed SnO_2 nanoparticles exhibit a blue-shift in comparison with those of bulk SnO_2, and the blue shift becomes increasingly significant with decreasing particle size. This may be ascribed to the variation of defect concentration, as it has been showed previously that defect structures within nanosized materials strongly affect the Raman scattering profiles by producing large blue shift and broadening of the spectral peaks [55, 56].

Figure 4 (left panel) shows the corresponding Raman scattering spectra in the low frequency range. Interestingly, for all the three particle samples, there are two broad peaks around 260 and 310 cm^{-1}, which are rarely observed in bulk SnO_2 materials. However, such low-frequency Raman

Fig. 2 Transmission electron micrographs of SnO$_2$ nanoparticles synthesized at different voltages: 20 V (**a**, **b**), 30 V (**c**, **d**), and 40 V (**e**, **f**). The left panels (**a**, **c**, and **e**) are the as-synthesized particles, whereas the right panels (**b**, **d**, and **f**) are particles that have undergone thermal sintering at 700 °C for 6 h. The scale bars are all 100 nm
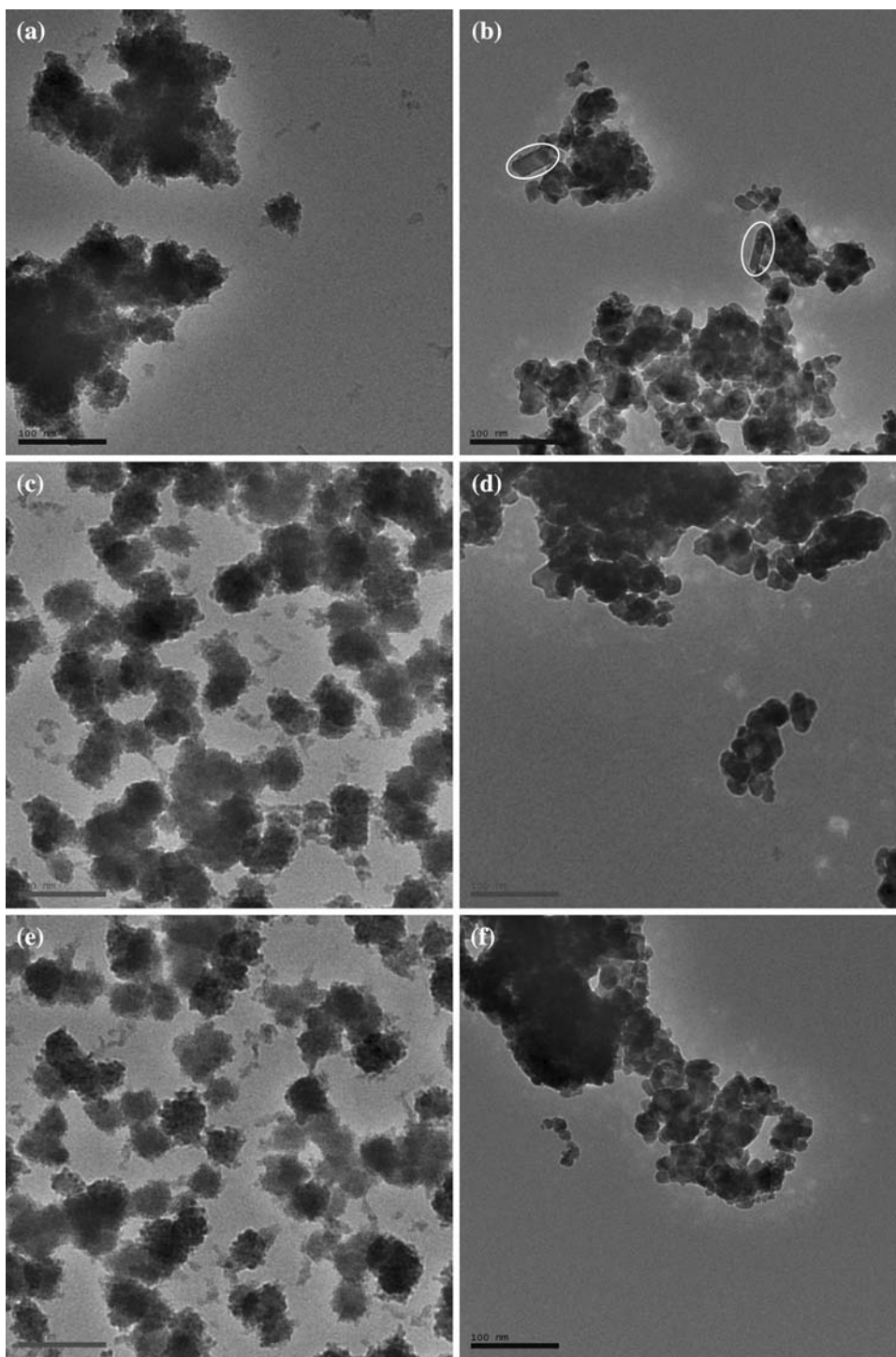
peaks have recently been reported with SnO$_2$ nanomaterials [52, 53]. It is usually accepted that some inactive modes in bulk materials can be rendered active in nanoparticles or other nanomaterials due to the size effect that breaks down the symmetry restriction. So the Raman bands that appear in the low frequency window may be ascribed to the active mode from the inactive E$_u$ TO mode (TO is the mode of transverse optical phonons) [52, 53, 57, 58].

Figure 5 shows the UV-visible spectra of the three annealed SnO$_2$ samples synthesized at different voltage. A narrow absorption band can be seen of all the three samples at the characteristic wavelength of about 304 nm, which is superimposed onto the exponential decay absorption profile, suggesting a narrow size distribution of the SnO$_2$ nanoparticles (cf. Figs. 2 and 3). While it is tempting to estimate the bandgap energy of the SnO$_2$ nanoparticles

Fig. 3 High-resolution transmission electron micrographs of SnO_2 nanoparticles synthesized at different voltages: 20 V (**a**, **b**), 30 V (**c**, **d**), and 40 V (**e**, **f**). The left panels (**a**, **c**, and **e**) are the as-synthesized particles, whereas the right panels (**b**, **d**, and **f**) are particles that have undergone thermal sintering at 700 °C for 6 h. The scale bars are all 5 nm. In panel (**d**), the dashed lines highlight the twin structure of the SnO_2 nanoparticles
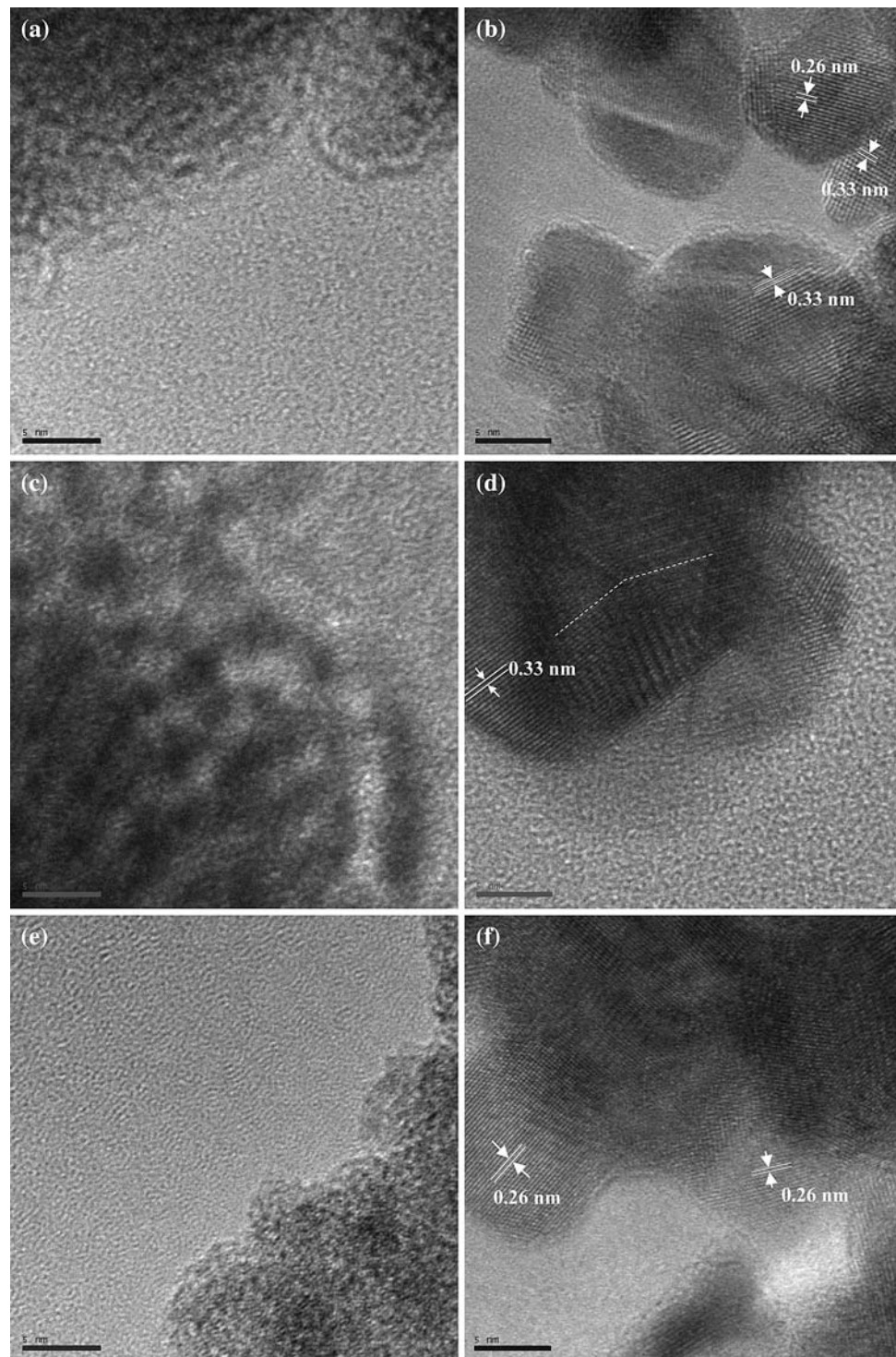
based on this absorption peak (4.08 eV), the particle core size of the annealed samples is actually too large to observe any quantum confinement effect as the Bohr radius of SnO_2 is merely 2.7 nm [39]. That is, the obtained particles are anticipated to behave like the bulk materials with a band-gap of 3.65 eV.

The room-temperature PL behaviors of the SnO_2 nanoparticles were also investigated and the results are shown in Fig. 6. It can be seen that when excited at 236 nm, the three annealed particle samples all exhibit a broad strong emission band that consists of a series of emission peaks located at 372, 420, 462, and 525 nm. It is well-known that

Fig. 4 Room-temperature Raman scattering spectra of the annealed SnO_2 nanoparticles that were initially synthesized at different voltages: 20, 30, and 40 V
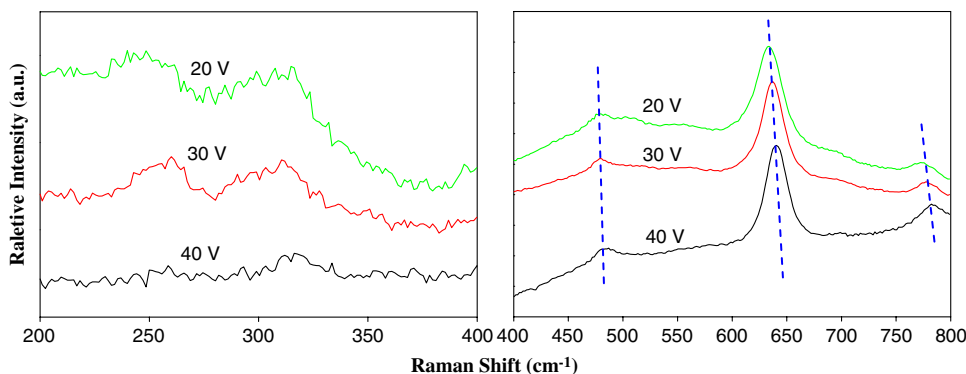
Table 2 Raman peak positions corresponding to the E_{1g}, A_{1g}, and B_{2g} vibration modes of SnO_2

Sample	E_{1g} (cm^{-1})	A_{1g} (cm^{-1})	B_{2g} (cm^{-1})
SnO_2 (bulk)[a]	474.0	632.0	774.0
SnO_2 (20 V)	479.0	633.7	774.1
SnO_2 (30 V)	479.5	636.8	777.6
SnO_2 (40 V)	484.4	640.8	782.5

[a] Data from Ref. [53]
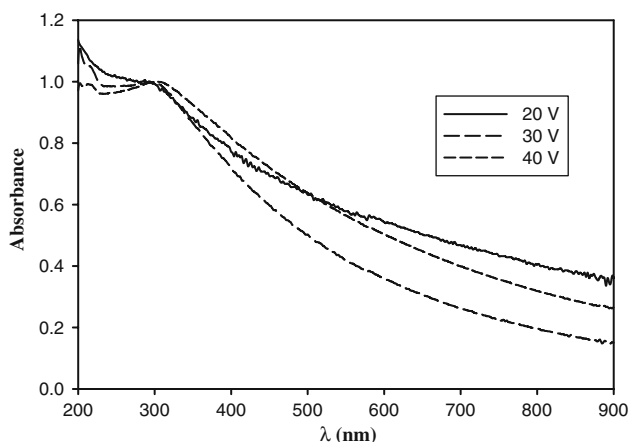
Fig. 5 UV-visible spectra of SnO_2 nanoparticles synthesized at different voltage (shown as figure legends) and annealed at 700 °C for 6 h

Fig. 6 Room-temperature photoluminescence spectra of the SnO_2 nanoparticles that were initially synthesized at different voltages, 20, 30, and 40 V, and annealed at 700 °C for 6 h. The excitation wavelength is 236 nm for all three samples

of oxygen vacancies [61]. A similar emission has also been reported in the photoluminescence studies on other SnO_2 nanomaterials [32, 63].

the visible light emissions of SnO_2 are related to the defect levels within the band gap, such as O vacancies and Sn interstitial sites formed during the particle growth [59, 60]. For instance, the peak at 372 nm is generally ascribed to the band-to-acceptor transition and related to the impurity or defect concentration [61]. The emission peak at 420 nm can be attributed to structural defects or luminescence centers, such as nanocrystals and defects in SnO_2 nanoparticles [61]. The peak at 462 nm is possibly from the electronic transition mediated by defect levels such as O vacancies in the band gap [62]. Finally, the 525 nm emission is likely to originate from oxygen vacancies where its intensity increases with increasing concentration

Conclusion

An effective electrochemical route has been developed for the preparation of SnO_2 nanoparticles whose dimensions can be controlled by the applied voltage. XRD measurements showed that whereas the as-prepared SnO_2 nanoparticles were amorphous, thermal sintering at 700 °C transformed the particles into a tetragonal rutile crystalline structure with abundant [101] and [211] orientations. Consistent results were observed in HRTEM measurements which exhibited well-defined crystalline lattice fringes. Further structural insights were obtained by varied spectroscopic measurements, such as Raman scattering, UV-Vis and photoluminescence spectroscopy. Three fundamental Raman peaks were identified which were ascribed to the E_{1g}, A_{1g}, and B_{2g} vibration modes, and the peak positions were found to blue-shift with the decrease of

particle size possibly as a consequence of the increasing concentration of defects in the particles. In addition, the particles all displayed a broad photoluminescence band consisting of various emission peaks. In short, the present work provides a simple and effective method for the large-scale synthesis of SnO_2 nanoparticles with controlled dimensions and structures. Further work is being carried out to examine their electronic characteristics which may have implications in energy conversion.

References

1. Ferrere S, Zaban A, Gregg BA (1997) J Phys Chem B 101:4490. doi:10.1021/jp970683d
2. Wang Y, Lee JY, Zeng HC (2005) Chem Mater 17:3899. doi:10.1021/cm050724f
3. Wang Y, Zeng HC, Lee JY (2006) Adv Mater 18:645. doi:10.1002/adma.200501883
4. Stampfl SR, Chen Y, Dumesic JA, Niu CM, Hill CG (1987) J Catal 105:445. doi:10.1016/0021-9517(87)90072-8
5. Zhang Y, Kolmakov A, Lilach Y, Moskovits M (2005) J Phys Chem B 109:1923. doi:10.1021/jp045509l
6. Nicholas CP, Marks TJ (2004) Nano Lett 4:1557. doi:10.1021/nl049255r
7. Wang YL, Jiang XC, Xia YN (2003) J Am Chem Soc 125:16176. doi:10.1021/ja037743f
8. Comini E, Faglia G, Sberveglieri G, Pan ZW, Wang ZL (2002) Appl Phys Lett 81:1869. doi:10.1063/1.1504867
9. Kolmakov A, Zhang YX, Cheng GS, Moskovits M (2003) Adv Mater 15:997. doi:10.1002/adma.200304889
10. Law M, Kind H, Messer B, Kim F, Yang PD (2002) Angew Chem Int Ed 41:2405. doi:10.1002/1521-3773(20020703)41:13<2405::AID-ANIE2405>3.0.CO;2-3
11. Huang J, Matsunaga N, Shimanoe K, Yamazoe N, Kunitake T (2005) Chem Mater 17:3513. doi:10.1021/cm047819m
12. Akari S, Friemelt K, Glockler K, Luxsteiner MC, Bucher E, Dransfeld K (1993) Appl Phys A Mater Sci Process 57:221
13. Tatsuyama C, Ichimura S (1976) Jpn J Appl Phys 15:843. doi:10.1143/JJAP.15.843
14. Cheng Y, Xiong P, Fields L, Zheng JP, Yang RS, Wang ZL (2006) Appl Phys Lett 89:093114. doi:10.1063/1.2338754
15. Yang YY, Pradhan S, Chen SW (2004) J Am Chem Soc 126:76. doi:10.1021/ja037675x
16. Leite ER, Weber IT, Longo E, Varela JA (2000) Adv Mater 12:965. doi:10.1002/1521-4095(200006)12:13<965::AID-ADMA965>3.0.CO;2-7
17. Pang GS, Chen SG, Koltypin Y, Zaban A, Feng SH, Gedanken A (2001) Nano Lett 1:723. doi:10.1021/nl0156181
18. Juttukonda V, Paddock RL, Raymond JE, Denomme D, Richardson AE, Slusher LE et al (2006) J Am Chem Soc 128:420. doi:10.1021/ja056902n
19. Jiang LH, Sun GQ, Zhou ZH, Sun SG, Wang Q, Yan SY et al (2005) J Phys Chem B 109:8774. doi:10.1021/jp050334g
20. Xu CK, Xu GD, Liu YK, Zhao XL, Wang GH (2002) Scr Mater 46:789. doi:10.1016/S1359-6462(02)00077-5
21. Vayssieres L, Graetzel M (2004) Angew Chem Int Ed 43:3666. doi:10.1002/anie.200454000
22. Liu YK, Zheng CL, Wang WZ, Yin CR, Wang GH (2001) Adv Mater 13:1883. doi:10.1002/1521-4095(200112)13:24<1883::AID-ADMA1883>3.0.CO;2-Q
23. Wang WZ, Xu CK, Wang GH, Liu YK, Zheng CL (2002) J Appl Phys 92:2740. doi:10.1063/1.1497718
24. Duan JH, Yang SG, Liu HW, Gong JF, Huang HB, Zhao XN et al (2005) J Am Chem Soc 127:6180. doi:10.1021/ja042748d
25. Ding ZF, Quinn BM, Haram SK, Pell LE, Korgel BA, Bard AJ (2002) Science 296:1293. doi:10.1126/science.1069336
26. Lou XW, Wang Y, Yuan CL, Lee JY, Archer LA (2006) Adv Mater 18:2325. doi:10.1002/adma.200600733
27. Yu JG, Guo HT, Davis SA, Mann S (2006) Adv Funct Mater 16:2035. doi:10.1002/adfm.200600552
28. Zhu W, Wang WZ, Xu HL, Shi JL (2006) Mater Chem Phys 99:127. doi:10.1016/j.matchemphys.2005.10.002
29. Xie J, Varadan VK (2005) Mater Chem Phys 91:274. doi:10.1016/j.matchemphys.2004.11.033
30. Duan XF, Lieber CM (2000) Adv Mater 12:298. doi:10.1002/(SICI)1521-4095(200002)12:4<298::AID-ADMA298>3.0.CO;2-Y
31. Morales AM, Lieber CM (1998) Science 279:208. doi:10.1126/science.279.5348.208
32. Wang B, Yang YH, Wang CX, Xu NS, Yang GW (2005) J Appl Phys 98:124303
33. Dai ZR, Gole JL, Stout JD, Wang ZL (2002) J Phys Chem B 106:1274. doi:10.1021/jp013214r
34. Liu Y, Dong H, Liu ML (2004) Adv Mater 16:353. doi:10.1002/adma.200306104
35. Mukhamedshina DM, Beisenkhanov NB, Mit KA, Valitova IV, Botvin VA (2005) High Temp Mater Process 9:307. doi:10.1615/HighTempMatProc.v9.i2.130
36. Minami T, Nanto H, Takata S (1988) Jpn J Appl Phys Part 2 Lett 27:L287
37. Ye CH, Fang XS, Wang YH, Xie TW, Zhao AW, Zhang LD (2004) Chem Lett 33:54. doi:10.1246/cl.2004.54
38. Han WQ, Zettl A (2003) Nano Lett 3:681. doi:10.1021/nl034142d
39. Zhu HL, Yang DR, Yu GX, Zhang H, Yao KH (2006) Nanotechnology 17:2386. doi:10.1088/0957-4484/17/9/052
40. Reetz MT, Helbig W (1994) J Am Chem Soc 116:7401. doi:10.1021/ja00095a051
41. Reetz MT, Helbig W, Quaiser SA (1995) Chem Mater 7:2227. doi:10.1021/cm00060a004
42. Talapin DV, Murray CB (2005) Science 310:86. doi:10.1126/science.1116703
43. Dierstein A, Natter H, Meyer F, Stephan HO, Kropf C, Hempelmann R (2001) Scr Mater 44:2209. doi:10.1016/S1359-6462(01)00906-X
44. Kamada K, Mukai M, Matsumoto Y (2002) Electrochim Acta 47:3309. doi:10.1016/S0013-4686(02)00251-7
45. Ruan CM, Paulose M, Varghese OK, Mor GK, Grimes CA (2005) J Phys Chem B 109:15754. doi:10.1021/jp052736u
46. Paulose M, Shankar K, Yoriya S, Prakasam HE, Varghese OK, Mor GK et al (2006) J Phys Chem B 110:16179. doi:10.1021/jp064020k
47. Tsuchiya H, Macak JM, Taveira L, Balaur E, Ghicov A, Sirotna K et al (2005) Electrochem Commun 7:576. doi:10.1016/j.elecom.2005.04.008
48. Yusta FJ, Hitchman ML, Shamlian SH (1997) J Mater Chem 7:1421. doi:10.1039/a608525c

49. Maestre D, Ramirez-Castellanos J, Hidalgo P, Cremades A, Gonzalez-Calbet JM, Piqueras J (2007) Eur J Inorg Chem 1544. doi:10.1002/ejic.200600990

50. Porto SPS, Fleury PA, Damen TC (1967) Phys Rev 154:522. doi:10.1103/PhysRev.154.522

51. Trayler JG, Smith HG, Nicklow RM, Wilkinson MK (1971) Phys Rev B 3:3457. doi:10.1103/PhysRevB.3.3457

52. Rumyantseva MN, Gaskov AM, Rosman N, Pagnier T, Morante JR (2005) Chem Mater 17:893. doi:10.1021/cm0490470

53. Sun SH, Meng GW, Zhang GX, Gao T, Geng BY, Zhang LD et al (2003) Chem Phys Lett 376:103. doi:10.1016/S0009-2614(03)00965-5

54. Peercy PS, Morosin B (1973) Phys Rev B 7:2779. doi:10.1103/PhysRevB.7.2779

55. Parker JC, Siegel RW (1990) Appl Phys Lett 57:943. doi:10.1063/1.104274

56. Aita CR (2007) Appl Phys Lett 90:213112. doi:10.1063/1.2742914

57. Abello L, Bochu B, Gaskov A, Koudryavtseva S, Lucazeau G, Roumyantseva M (1998) J Solid State Chem 135:78. doi:10.1006/jssc.1997.7596

58. Dieguez A, Romano-Rodriguez A, Vila A, Morante JR (2001) J Appl Phys 90:1550. doi:10.1063/1.1385573

59. Cheng B, Russell JM, Shi WS, Zhang L, Samulski ET (2004) J Am Chem Soc 126:5972. doi:10.1021/ja0493244

60. Hu JQ, Bando Y, Liu QL, Golberg D (2003) Adv Funct Mater 13:493. doi:10.1002/adfm.200304327

61. Jeong J, Choi SP, Chang CI, Shin DC, Park JS, Lee BT et al (2003) Solid State Commun 127:595. doi:10.1016/S0038-1098(03)00614-8

62. Yu D, Wang CJ, Wehrenberg BL, Guyot-Sionnest P (2004) Phys Rev Lett 92:216802. doi:10.1103/PhysRevLett.92.216802

63. Wang B, Yang YH, Wang CX, Yang GW (2005) Chem Phys Lett 407:347. doi:10.1016/j.cplett.2005.03.119